Creep behavior of a precipitation-strengthened A2-B2 refractory high entropy alloy

Liu Yang[a], Sandipan Sen[a*], Daniel Schliephake[a], Raja J. Vikram[a], Stephan Laube[a], Aparajita Pramanik[b], Ankur Chauhan[b], Martin Heilmaier[a] and Alexander Kauffmann[a*]

[a] Institute for Applied Materials (IAM-WK), Karlsruhe Institute of Technology (KIT), Engelbert-Arnold-Str. 4, 76131 Karlsruhe, Germany

[a] Extreme Environments Materials Group, Department of Materials Engineering, Indian Institute of Science, Bengaluru, Karnataka 560012, India

* corresponding authors

mail: sandipan.sen@kit.edu (S. Sen)
mail: alexander.kauffmann@kit.edu (A. Kauffmann)
phone: +49 721 608 42346

Highlights

- Ta-Mo-Ti-Cr-Al with two-phase A2+B2 microstructure exhibits competitive creep resistance
- Precipitation strengthening by B2 precipitates in A2 matrix is effective even close to solvus
- N-type rafting is obtained for grains with close to ⟨100⟩ parallel to the loading direction

Abstract

Refractory high entropy alloys (RHEA) consisting of a disordered A2 matrix and ordered B2 precipitates mimic the microstructures of state-of-the-art, Ni-based superalloys with A1 matrix and $L1_2$ precipitates. They are promising candidates for high-temperature applications because of their high melting points. 27.3Ta-27.3Mo-27.3Ti-8Cr-10Al (in at. %) is a relevant example where this A2-B2, two-phase microstructure is formed by a precipitation reaction and remains stable even at temperatures close to the precipitate solvus temperature (T_S). The present study systematically addresses the creep response of poly-crystalline 27.3Ta-27.3Mo-27.3Ti-8Cr-10Al at temperatures of 1000 °C and above. Compared to poly-crystalline, single-phase A2 and B2 RHEA, a substantially higher creep resistance is observed for the two-phase alloy while minimum creep rates comparable to those of state-of-the-art single-crystalline A1-$L1_2$ CMSX-4 are found. This is specifically remarkable considering its poly-crystalline condition, the open matrix A2 crystal structure and extremely high homologous temperature of 0.98 T_S compared to 0.85 T_S for CMSX-4. Consistent with a positive lattice misfit, directional coarsening of precipitates is revealed in 27.3Ta-27.3Mo-27.3Ti-8Cr-10Al perpendicular to the compression direction after creep in grains with ⟨100⟩ close to the compression direction.

Keywords

Refractory high entropy alloys, compositionally complex alloys, super alloys, creep, high temperature

1. Introduction

The concept of high entropy alloys (HEA) has attracted the attention of many researchers since its introduction in the early 2000s by Yeh et al. [1,2] and Cantor et al. [3]. While HEA synthesized from 3d transition metals like Fe, Cr, Ni, Co and others have been of particular interest with respect to mechanical properties at ambient and low temperatures, the concept was soon extended to refractory high entropy alloys (RHEA) by the seminal work of Senkov et al. [4–7]. RHEA are composed of refractory elements and exhibit usually high melting points beyond 2000°C leading to excellent strength even up to 1600 °C [5]. As all refractory elements suffer from catastrophic oxidation at intermediate and high temperatures [8], concepts to improve their oxidation resistance were developed and introduced by adding potentially passivating elements like Al, Cr, etc. [9–12]. Particularly, RHEA containing Ta, Cr and Ti were identified to provide a strategy to achieve oxidation resistance by the formation of a slowly growing rutile type oxide [8,12–15]. Even though this protective oxide does not contain Al, Al promotes its formation and is thus added as a required element in the alloys [14]. Furthermore, Al and Ti lead to a significant reduction of density [16–18] as compared to RHEA composed of only refractory elements. When synthesized in close to equimolar composition and subjected to high-temperature homogenization treatments, most of the alloys from the Ta-Mo-Nb-Cr-Ti-Al system form almost single-phase material with disordered, body centered cubic (BCC) A2 (Strukturbericht designation) or ordered B2 crystal structure and low amounts of secondary phases [16–20].

Recently, considerable effort has been placed on advanced alloying strategies in non-equimolar, complex alloys (RCCA) to mimic the microstructures of state-of-the-art, Ni-based superalloys with Strukturbericht A1 (face centered cubic, FCC) matrix and $L1_2$ precipitates. The analogous microstructure in RCCA consists of a disordered A2 matrix and ordered B2 precipitates and the class of alloys is often referred to as refractory (or BCC) superalloys [21]. A huge variety of experimental [22–25] and theoretical considerations [26] were made to deliberately synthesize the A2-B2 microstructure. Particularly, within the Ta-Mo-Cr-Ti-Al system, alloys were identified that form the desired A2-B2 microstructures by a nucleation and growth process and the relevant reaction sequence of phase separation and ordering [27,28].

In view of recent systematic creep studies by Gadelmeier et al. [29] and Liu et al. [30], this type of microstructural tailoring aimed at efficient precipitation strengthening seems imperative to achieve competitive creep performance over established high temperature materials. In these works, the single-phase A2, equimolar TiHfNbTaZr was investigated with respect to its tensile creep behavior at 980 °C (50 – 120 MPa) and 1100 °C (10 – 30 MPa) [29,30]. The minimum creep rate at both temperatures was higher than 10^{-7} s^{-1} and thus creep resistance is notably lower than that of a state-of-the-art, precipitation-strengthened, single-crystalline Ni-based superalloy (e.g., CMSX-4 with a $L1_2$ solvus temperature of approximately 1280 °C [31]). This discrepancy is not only attributed to the poly-crystalline microstructure of HfNbTaTiZr, but also to the presence of a single-phase microstructure with solid solution strengthening only (absence of precipitation strengthening) as well as the commonly accepted faster diffusion in the non-closed packed A2 crystal structure. Furthermore, the microstructure was found to undergo a decomposition into A2 and A3 during creep [29].

Apart from the fundamental consideration of precipitation strengthening of an A2 matrix alloy by B2 precipitates, the detailed analysis of the microstructures after creep of the benchmark A1-$L1_2$ Ni-based superalloys has revealed significant microstructural changes induced by the creep deformation, the most prominent of which is rafting [32]. Rafting is a phenomenon of directional coarsening of the precipitates

during creep deformation. A rafted microstructure is essential to maintain high creep resistance at high-temperature and low stress condition, which can increase the dislocation climb distance at the interface between $L1_2$ and A1 [33]. The lattice misfit at the interface between precipitate and matrix not only plays an important role in the formation of the rafted microstructure, but also affects the directional relationship between the rafted microstructure and the external stresses [34]. This lattice misfit for the discussed system (in analogy to the Ni-based superalloy case) can be quantified by the following equation:

$$\delta = \frac{2(a_{B2} - a_{A2})}{a_{B2} + a_{A2}} \quad (1)$$

where, δ represents the lattice misfit, while a_{A2} and a_{B2} represent the lattice parameters of A2 and B2, respectively.

Table 1 shows the correlation between the sign of lattice misfit δ $(+/-)$, loading direction (tensile/compression) and the type of rafting (perpendicular/parallel to the applied uniaxial stress) observed during creep of A1-$L1_2$ Ni- and Co-based superalloys. When an alloy with a negative δ $(-)$ is subjected to tensile creep $(+)$ (i.e. the sign of the lattice misfit and the loading type are opposite to each other), the rafting direction of the $L1_2$ precipitates is reported to be perpendicular to the loading direction, which is known as N-type rafting [35]. Similarly, when an alloy with negative δ $(-)$ is subjected to compression creep stress $(-)$ (i.e. the sign of the lattice misfit and the loading type are same as each other), the rafting direction of the precipitates is parallel to the loading direction, which is known as P-type rafting [35]. It has to be noted that most of the studies focused on single crystalline (SX) superalloys and the creep was performed with uniaxial stress along the $\langle 001 \rangle$ direction. Even in the studies involving poly-crystals (PX), the N-type rafting was observed only for grains with close to $\langle 001 \rangle$ direction parallel to the loading direction [36]. A schematic for this relationship between the sign of δ and the type of uniaxial loading as reported for Ni- and Co- based superalloys is shown in Fig. 1.

Table 1. Dependence of the directional relationship between the loading direction and the rafted microstructure in Ni- and Co-based A1-$L1_2$ superalloys on the sign of lattice misfit δ (+/−) and uniaxial loading type (+, tension/−, compression).

Base	Designation	SX/PX	Misfit	Loading Type	Rafting Type	Ref.
Ni	ERBO 1	SX	−	+	Perpendicular (N)	[34]
	TMS-75				Perpendicular (N)	[35]
	LEK 94				Perpendicular (N)	[36]
	M951G	PX	−	+	Perpendicular (N)	[40]
	IN738LC		+	−	Perpendicular (N) at high stress positions for a conical compression sample	[41]
Co	Co-Al-W	SX	+	+	Parallel (P)	[39]
	Co-Al-W-Ta-Ti				Parallel (P)	[40]
	Co-Al-W-B			−	Perpendicular (N)	[44]
	Co-Al-W-B	PX	+	−	Perpendicular (N) only in $\langle 100 \rangle$ parallel to loading axis	[42], [43]

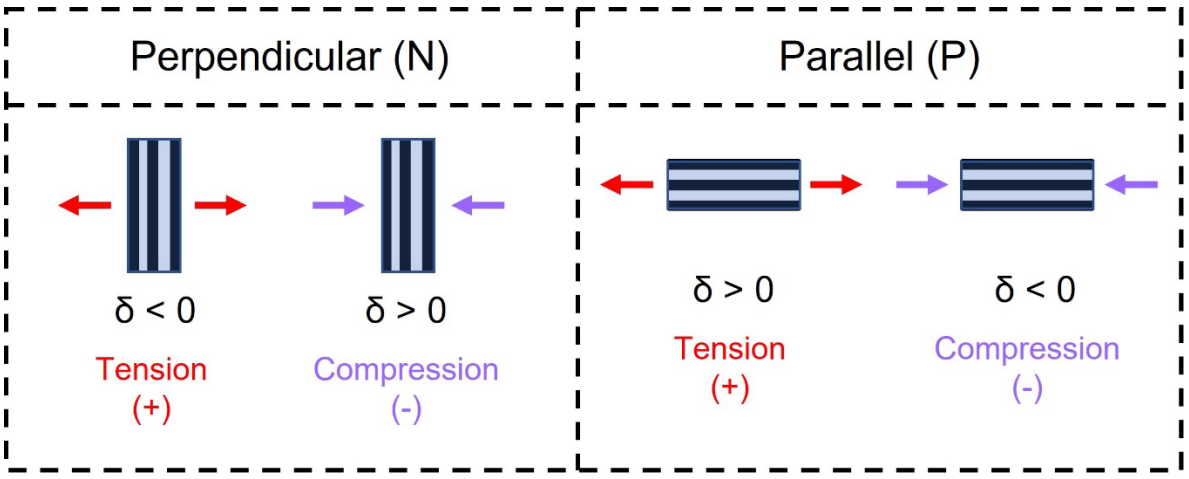

Fig. 1. The schematic of the dependence of rafting direction on the sign of lattice parameter δ and loading direction in Ni- and Co-based superalloys.

Despite the considerable efforts to develop A2-B2 RCCA, there is currently no systematic assessment of the creep behavior and mechanisms of such alloys as well as the impact of creep deformation on the A2-B2 microstructure available in literature. Thus, we present a first systematic study on the creep behavior of 27.3Ta-27.3Mo-27.3Ti-8Cr-10Al (in at. %, abbreviated by TMT-8Cr-10Al in what follows) as a model alloy introduced by Laube et al. [27,28]. It has been confirmed via differential scanning calorimetry (DSC) that B2 precipitates form by a diffusion-controlled precipitation below temperatures of around 1055 °C [27]. Additionally, a stable two-phase microstructure was found even after prolonged exposure at temperatures close to the solvus temperature [28]. These findings suggest promising prospect for achieving high-temperature creep resistance in this alloy.

In detail, we focus on the following fundamental research questions:

1. How does the creep behavior of a two-phase, precipitation-strengthened A2-B2 TMT-8Cr-10Al compares to that of state-of-the-art, single-crystalline Ni-based superalloys with A1-$L1_2$ microstructure as well as to poly-crystalline, single-phase A2 or B2 RHEA?
2. How does the microstructure of TMT-8Cr-10Al evolves during the creep loading?
3. How do the microstructural changes depend on the coherency and lattice misfit between the B2 precipitates and the A2 matrix?

2. Experiments and Materials

TMT-8Cr-10Al was synthesized by repetitive arc melting under Ar atmosphere using an AM/0.5 furnace supplied by Edmund Bühler GmbH (Germany). The purities of the elements Ta, Mo, Ti, Cr, and Al provided by chemPUR GmbH (Germany), were 99.9%, 99.95%, 99.8%, 99.99%, and 99.99%, respectively. One button, weighing approximately 150 g, was synthesized by five steps of flipping and re-melting. The button was then cast into a cuboid shape using a water-cooled Cu mold. Subsequently, the as-cast TMT-8Cr-10Al alloy was wrapped in Mo foil (to prevent any forms of oxidation) for homogenization at 1600 °C for 20 h to remove the as-cast dendritic microstructure at a heating and cooling rate of 100 K/h in a HTRT 70-600/18 resistance tube furnace (Carbolite Gero GmbH & Co. KG, Germany) with three evacuation cycles and backfilling with continuous Ar flow in order to prevent oxidation. Further details on the synthesis process can be found in previous studies [27,28].

To investigate the microstructure, samples were cut from the button by electrical discharge machining (EDM) were first ground with SiC abrasive paper to P4000 grit. Afterwards, 3 µm and 1 µm poly-crystalline diamond suspension were used for polishing for 5 min each. Then, the samples were polished for 10 min using a colloidal oxide polishing suspension provided by Buehler ITW (Germany) on a semi-automatic machine. The final preparation step was chemo-mechanical vibratory polishing using a non-crystallizing oxide polishing suspension provided by Struers (Germany) for at least 16 h. Scanning electron microscopy (SEM) was performed using on a Zeiss LEO 1530 (Zeiss, Germany) at 20 kV acceleration voltage. Electron backscatter diffraction (SEM-EBSD) with an EDAX Digiview system (Ametek, USA) in a Zeiss Auriga 60 (Zeiss, Germany) was used to image the local crystallographic orientation and to identify secondary phases. Composition was determined by inductively coupled plasma-optical emission spectroscopy (ICP-OES) of the homogenized TMT-8Cr-10Al alloy and scanning electron microscopy-based energy dispersive X-ray spectroscopy (SEM-EDS) in the Zeiss Auriga 60 system with Octane Super-A detector (Ametek, USA). The levels of O and N impurities were detected in five samples of the TMT-8Cr-10Al by hot carrier gas extraction (HCGE) utilizing a TC500 system supplied by Leco Instrumente GmbH, Germany. The density of the alloy was calculated according to Archimedes' principle by selecting five samples to calculate the average density. The density measurements were conducted with the weighing machine ME204T/00 with a density measuring kit ME-DNY-43 from the company Mettler-Toledo GmbH (Germany).

For transmission electron microscopy (TEM), electron-transparent foils were prepared using a lift-out technique with a ThermoFisher Scios-2 (USA) system equipped with a dual beam focused ion beam (FIB). Initially, a protective platinum layer was deposited, followed by FIB sectioning at 30 kV with probe currents of 5 nA and 1 nA, respectively. The TEM lamellae were then lifted out and attached to a molybdenum half-grid through platinum deposition. Subsequently, the lamellae were thinned to approximately 80 nm using various voltage and current combinations in the FIB. Final cleaning was performed at 2 kV and 10 pA for an extended period.

Diffraction contrast imaging was performed using a ThermoFisher Tecnai T20-ST (USA) TEM operated at 200 kV in parallel illumination mode. The atomic structure of the phases was investigated using scanning transmission electron microscopy (STEM) in a probe-corrected ThermoFisher Titan Themis (USA) TEM operated at 300 kV. The TEM foil was tilted to a low-index zone axis for diffraction contrast and atomic resolution imaging. Atomic resolution micrographs were acquired with a high-angle annular dark field (HAADF) detector and a camera length of 160 mm. Specimen drift during atomic resolution imaging was corrected using the drift-corrected frame integration (DCFI) function of Velox software. Lattice parameters of the phases were estimated by filtering a specific reflection in the fast Fourier transformation (FFT) of the high-resolution HAADF-STEM micrographs and measuring interplanar spacing with the line profile tool in Gatan Microscopy Suite software.

The samples for compression creep tests with dimensions of ($5 \times 3 \times 3$) mm^3 were prepared by electrical discharge machining (EDM). Before creep testing, the surface of each sample was ground to remove the oxidation/EDM layer. Compression creep tests were carried out under vacuum (to exclude environmental effects on creep) utilizing a Z100 electro-mechanical universal testing machine provided by ZwickRoell GmbH & Co. KG (Germany) equipped with a vacuum furnace supplied by Maytec GmbH (Germany). The test temperatures ranged from 1000 °C to 1060 °C and true stresses of 75 MPa, 100 MPa and 125 MPa were applied. All compression creep tests were started after a duration of 30 min under a preload 50 N at the test temperature to ensure uniform temperature distribution. After the creep test, the samples were cooled to room temperature by furnace cooling and then prepared for

microstructural investigations using the metallographic steps described above. At least three tests were performed at each test condition in order to ensure the relevance of the results. In order to track the impact of long-term heat treatment under the same conditions without external mechanical load, stress-free heat treatments were also performed at the same temperatures and durations compared to the compression creep tests. The samples used for heat treatment were wrapped in Ta foil and then sealed into fused silica tubes under Ar atmosphere to avoid oxidation during the heat treatment process. After quenching, microstructural studies were carried out on the heat-treated samples following the above-mentioned metallographic steps.

3. Results and Discussion

3.1 Initial Composition and Microstructure

In order to assess the chemical composition of TMT-8Cr-10Al, ICP-OES and HCGE were conducted and the results are shown in Table 1. The composition of the constituent elements observed via ICP-OES is within the experimental accuracy range. The levels of O and N are found to be between 100 and 500 wt.-ppm and are comparable to other studies in RHEA [27,46–48]. The chemical homogeneity of this alloy at the microscale determined by SEM-EDS was reported previously [27]. The experimental density of the alloy determined by the Archimedes method is 9.6 g.cm^{-3}.

Table 2. Composition, impurity levels and density of the homogenized TMT-8Cr-10Al.

	Composition in at. %					**Impurities in wt.-ppm**		**Density in g·cm^{-3}**
	Ta	Mo	Ti	Cr	Al	O	N	
Target	27.3	27.3	27.3	8	10	–	–	
Experimental	26.0	29.8	27.4	7.3	9.4	352 ± 88	45 ± 14	9.6

Fig. 2 (a) shows an inverse pole figure (IPF) map of the TMT-8Cr-10Al obtained by SEM-EBSD in the as-homogenized condition. It can be observed that the orientation of the grains is random indicating no preferred orientation present in the initial microstructure. In the orientation-contrast SEM-BSE micrographs, a coarse-grained microstructure as well as some pores (displayed as dark features) are revealed, as shown in Fig. 2 (b). The appearance of pores is due to the Kirkendall effect that occurs during homogenization of dendritic cast microstructures with significant Al enrichment in the interdendritic regions [49]. The mean grain size of the investigated samples is above 200 µm. At higher magnification, two different SEM-BSE contrasts within the grains at the nanoscale can be observed as shown in Fig. 2 (c). Those contrasts are attributed to the difference in atomic number *Z* between A2 and B2. The composition of these phases was reported earlier [27], the continuous bright matrix is enriched in Ta and Mo while the dark precipitates are enriched in Al and Ti, with Cr distributed uniformly throughout the alloy. The bright matrix phase was identified as a disordered A2 and the discontinuous dark phase as ordered B2 precipitates via TEM experiments in Refs. [27], [28]. Additional dark particles (marked with white arrows in (c)) of less than 0.1 vol.% were also observed at grain boundaries, which were previously identified to be Ti-rich nitrides resulting from N contamination during arc melting and homogenization [28].

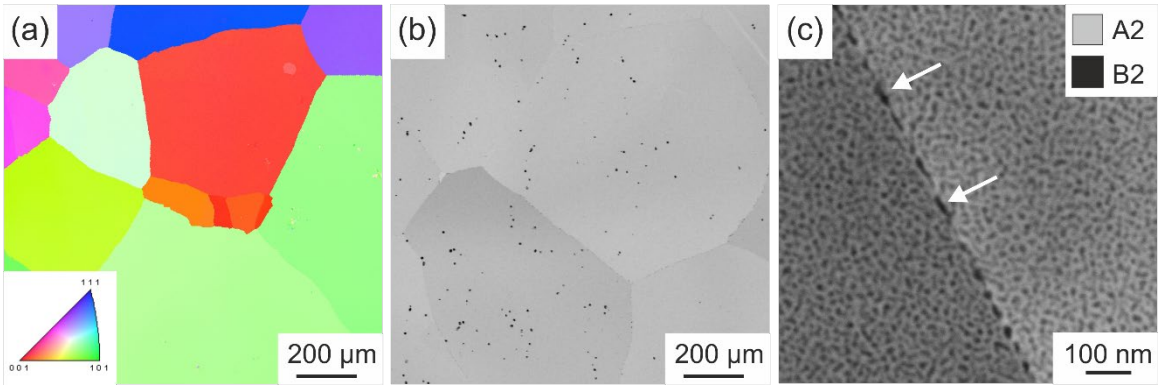

Fig. 2. Microstructure of TMT-8Cr-10Al after homogenization at 1600 °C for 20 h: (a) IPF map (color code in the inset). (b-c) SEM-BSE micrographs at different magnification.

In order to determine the coherency relationship between the A2 matrix and B2 precipitates, TEM investigation was performed on a sample heat-treated at 1000 °C for 1000 h with a microstructure coarsened under similar conditions compared to the creep investigations discussed later in this article. Figure 3a shows a dark-field (DF) micrograph with bright-contrast plate-like precipitates uniformly distributed throughout the matrix consistent with the SEM-BSE images shown in Fig. 2 (c). The inset displays the corresponding indexed selected area electron diffraction (SAED) pattern acquired along the $\langle 011 \rangle$ zone axis from this region. The DF micrograph was obtained using a (weak) $\{100\}$ superlattice spot at half the distance of the $\{200\}$ A2 fundamental peaks, indicating the presence of the long-range ordered phase. The superlattice spots correspond to the B2 phase. Fig. 3 (b) and Fig. 3 (c) present atomic resolution STEM micrographs taken near the $\langle 011 \rangle$ zone axis of the matrix and precipitate, respectively. These micrographs reconfirm that the matrix and precipitates have A2 and B2 crystal structure, respectively. The lattice parameters of the matrix a_{A2} and precipitate a_{B2} were estimated to be 0.315 and 0.322 nm, respectively. From that, the lattice misfit parameter δ between the A2 matrix and B2 phase with $\{100\}_{A2} \parallel \{100\}_{B2}$ and $\langle 001 \rangle_{A2} \parallel \langle 001 \rangle_{B2}$ is determined to be positive with a value of +0.022 according to Eq. 1.

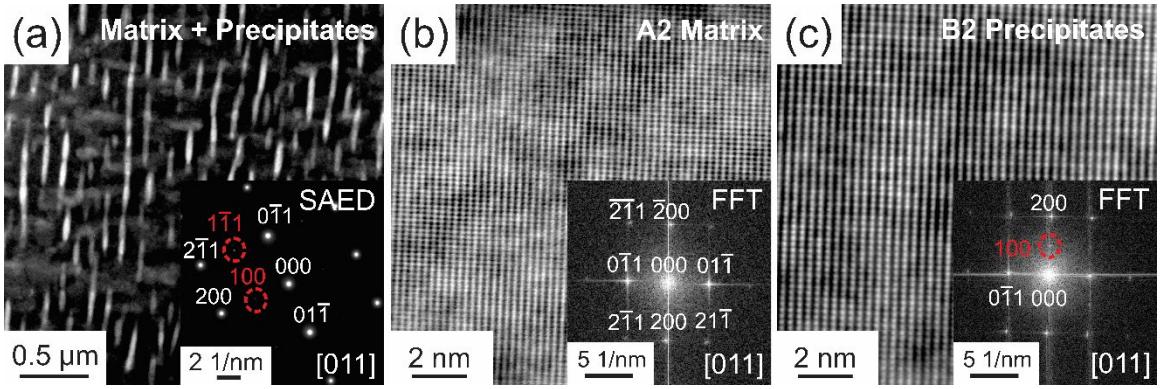

Fig. 3. TEM results of the TMT-8Cr-10Al alloy after heat treatment at 1000 °C for 1000 h: (a) DF TEM micrograph showcasing bright contrast B2 precipitates uniformly distributed throughout the matrix. The micrograph was acquired using a $\{100\}$ superlattice spot in the corresponding SAED pattern taken along a $\langle 011 \rangle$ zone axis from this region (inset). (b) Atomic resolution micrograph of the matrix with its corresponding FFT in the inset. (c) Atomic resolution micrograph of a B2 precipitate with its corresponding FFT in the inset.

3.2 Creep Behavior

To understand the creep behavior of TMT-8Cr-10Al, creep tests were conducted at (1000 ± 5) °C and 125 MPa, i.e. about 50 K below the reported solvus temperature of TMT-8Cr-10Al [27]. In order to

study the relationship of creep strain with respect to time and to check its reproducibility for a precipitation strengthened microstructure, three different creep tests under the same conditions were conducted with each test being interrupted at different strains. To study the evolution of the creep rate with increasing temperature, the creep temperature was varied between 1000 to 1060 °C, keeping the applied true stress at 125 MPa.

Fig. 4 (a) shows the compression creep curves of TMT-8Cr-10Al with respect to time for total strains of 0.5%, 0.6% and 0.8%. The creep rate at the end of each test was found to be approximately $2.5 \cdot 10^{-9}$ s^{-1}. In order to visualize the creep rate for these three tests, the logarithm of creep rate vs. creep strain was plotted as shown in Fig. 4 (b) with blue lines (dashes and dotted) ending in an open circle symbol. Fig. 4 (b) also shows the variation of the true creep rate vs. creep strain with solid lines ending in an open circle symbol for tests at different temperatures (higher than 1000 °C) and a constant stress of 125 MPa.

It is relevant to note here that between the curves for 1000 and 1030 °C (a difference of 30 K), the minimum creep rate jumps by one order of magnitude. However, between 1030 °C and 1040 °C (a difference of 10 K), the minimum creep rate changes by one order of magnitude signifying a significant reduction in the creep resistance between 1030 and 1040 °C. This can also be observed from the values in Table 2 that the $\dot{\varepsilon}_{min}$ substantially increases (which indicates a reduction in creep resistance) between 1030 and 1040 °C. These two regions, ≤ 1030 °C and ≥ 1040 °C, are demarcated as high creep resistance (HCR) regime which exhibits a good creep resistance and the low creep resistance (LCR) regime where the creep resistance is notably lower. These two regions are highlighted by blue and red lines or symbols.

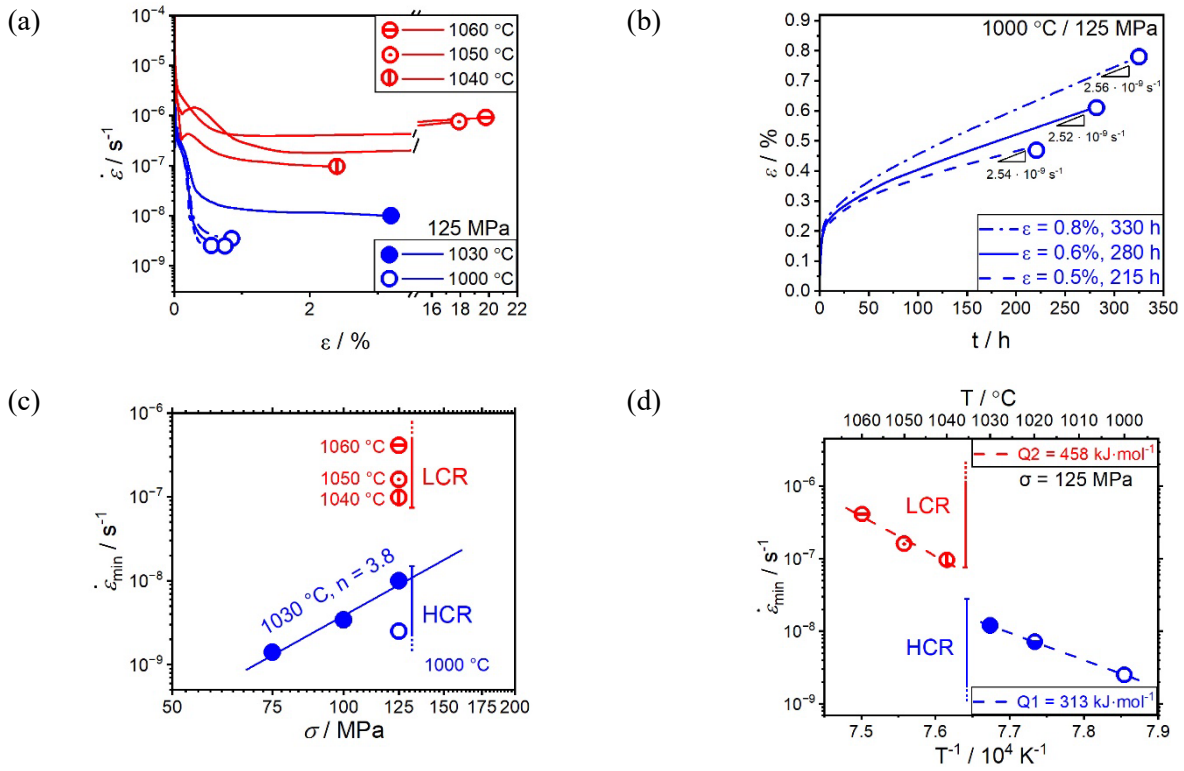

Fig. 4. Creep behavior of TMT-8Cr-10Al: (a) creep strain ε as a function of time t for 125 MPa and 1000 °C condition. (b) Logarithmic plot of strain rate $\dot{\varepsilon}$ vs. strain ε for 125 MPa at different temperatures. (c) Arrhenius plot for 125 MPa. (d) Norton plot. The creep regimes are demarcated as High Creep Resistance (HCR) marked in blue and Low Creep Resistance (LCR) depicted in red.

Here, a distinction has to be noted between steady state creep rate ($\dot{\varepsilon}_{\mathrm{steady}}$) and minimum creep rate ($\dot{\varepsilon}_{\mathrm{min}}$). In order to qualify for a mechanical [50] or even microstructural steady state [51], a substantial plastic strain release should be obtained in the period of constant strain rate. All the three tests performed at 1000 °C do not reach a steady state according to this definition. However, the creep tests performed at temperatures higher than 1000 °C reveal this steady state creep clearly. It must be noted that a steady state regime at 1000 °C could, in principle, be experimentally verified but a plastic strain release of for example 5% would take close to 200 days. Based on the creep curve exhibiting a steady state regime at 1030 °C (full blue circle in Fig. 4, where the A2-B2 microstructure is still stable), we can infer that the creep rate of $2.5 \cdot 10^{-9}$ s^{-1} at 1000 °C might also be regarded as the steady state creep rate. Unlike the creep curves for A1-$L1_2$ superalloys [33], the $\dot{\varepsilon}_{\mathrm{steady}}$ observed for the TMT-8Cr-10Al at all temperatures are also incidentally the $\dot{\varepsilon}_{\mathrm{min}}$. Hence, for the discussion that follows next, we will denote the $\dot{\varepsilon}_{\mathrm{steady}}$ as $\dot{\varepsilon}_{\mathrm{min}}$, since both are essentially the same for the TMT-8Cr-10Al alloy and it enables us to make a direct comparison to the creep behavior of other materials.

Table 2. $\dot{\varepsilon}_{\mathrm{min}}$ of TMT-8Cr-10Al measured at 125 MPa with different temperatures.

σ / MPa			**125**		
T / °C	1000	1030	1040	1050	1060
$\dot{\varepsilon}_{\mathrm{min}}$ **/ s^{-1}**	$2.5 \cdot 10^{-9}$	$1.0 \cdot 10^{-8}$	$9.6 \cdot 10^{-8}$	$1.6 \cdot 10^{-7}$	$4.1 \cdot 10^{-7}$

The logarithm of $\dot{\varepsilon}_{\mathrm{min}}$ for all temperatures is plotted in Fig. 4 (c) against the inverse of the temperature according to the Mukherjee-Bird-Dorn equation [52]:

$$\dot{\varepsilon}_{\mathrm{min}} = A \frac{D_0 G b}{k T} \left(\frac{b}{d}\right)^p \left(\frac{\sigma}{G}\right)^n \exp\left(-\frac{Q}{k T}\right) \quad (2)$$

where, $\dot{\varepsilon}_{\mathrm{min}}$ is the minimum creep rate, A the Dorn constant, D_0 a pre-exponential factor, G the shear modulus, b the Burgers vector, k the Boltzmann constant, T the temperature, d the grain size, p the inverse grain size exponent, σ the applied stress, n the stress exponent, Q the activation energy. A linear dependence is obtained.

For TMT-8Cr-10Al, two different parts of the linear fit can be observed. For each part of the Arrhenius plot, two distinct, apparent activation enthalpy values (Q) can be evaluated. These two regimes incidentally also fall in the ranges of ⩽1030 and ⩾1040 °C, in line with the demarcation suggested for Fig. 4 (b). Hence the color scheme of blue and red for ⩽ 1030 and ⩾1040 °C, respectively, has been maintained for Fig. 4 (c). The apparent activation energy for creep was determined to be 313 kJ/mol in the temperature range of HCR and 458 kJ/mol in the temperature range of LCR. For pure metals, a possible correlation between the apparent activation enthalpy observed during creep and the activation enthalpy for the self-diffusion of the metal atoms was reported [53]. However, this straightforward correlation becomes difficult when multi-component, single phase or even multi-phase materials are addressed [54]. Considering that TMT-8Cr-10Al not only has five principal elements but also two different phases along with grain boundaries, the correlation of the obtained activation enthalpy for creep with the activation enthalpy for the self-diffusion of the constituent elements is not trivial.

In order to determine the apparent stress exponent n according to Eq. (2) [52], creep tests were conducted at 1030 °C at three different stresses of 75, 100 and 125 MPa. The results are shown in Fig. 4 (d). The n value is determined by plotting the logarithm of minimum creep rate at constant temperature against the different applied stresses. The apparent stress exponent n determined by linear

fitting is 3.8. When compared to pure metals and single-phase alloys, n values between 3 and 5 indicate dislocation climb as the rate controlling process of creep [55]. It should be noted that similar to the activation enthalpy discussed earlier, the evaluated n is an apparent quantity. This is due to the fact that the observed creep behavior is an effective behavior potentially involving dislocation glide, dislocation climb as well as grain boundary sliding in TMT-8Cr-10Al. Similar to the activation enthalpy, a simple comparison to single-phase metals or alloys might lead to a false conclusion without proper microstructural evidence for the active micromechanical mechanisms.

For a precipitation strengthened material like TMT-8Cr-10Al, it is imperative to compare the macro-mechanical properties like creep with other high temperature alloys. Fig. 5 shows the creep results of our poly-crystalline TMT-8Cr-10Al consisting of A2 matrix and B2 precipitates as compared to those of single-crystal Ni-based superalloy CMSX-4 with A1 matrix and $L1_2$ precipitates [56,57], poly-crystalline single-phase, A2 TiZrHfNbTa [29] and single-phase B2 NbMoCrTiAl [58]. The minimum creep rates at low stresses of 100 to 200 MPa of poly-crystalline TMT-8Cr-10Al at 1030 °C are comparable to that of single-crystalline CMSX-4 at 1050 °C as can be seen in Fig. 5. It must be noted that TMT-8Cr-10Al tested at 1030 °C is operated much closer to the reported solvus temperature of the B2 precipitates (T_S) of 1055 °C (0.98 T_S) compared to that in the case CMSX-4 tested at 1050 °C with a solvus temperature of $L1_2$ of 1280 °C (0.85 T_S). At comparable temperatures and stresses, TMT-8Cr-10Al has a minimum creep rate about four orders of magnitude lower than both, the single-phase A2 TiZrHfNbTa alloy and the single-phase B2 NbMoCrTiAl alloy, which undergoes a microstructural decomposition to a multi-phase intermetallic microstructure during creep [58]. This reaffirms the substantial impact of precipitation strengthening achieved in TMT-8Cr-10Al and provides a pathway for developing RHEA with a two-phase microstructure in high-temperature creep applications.

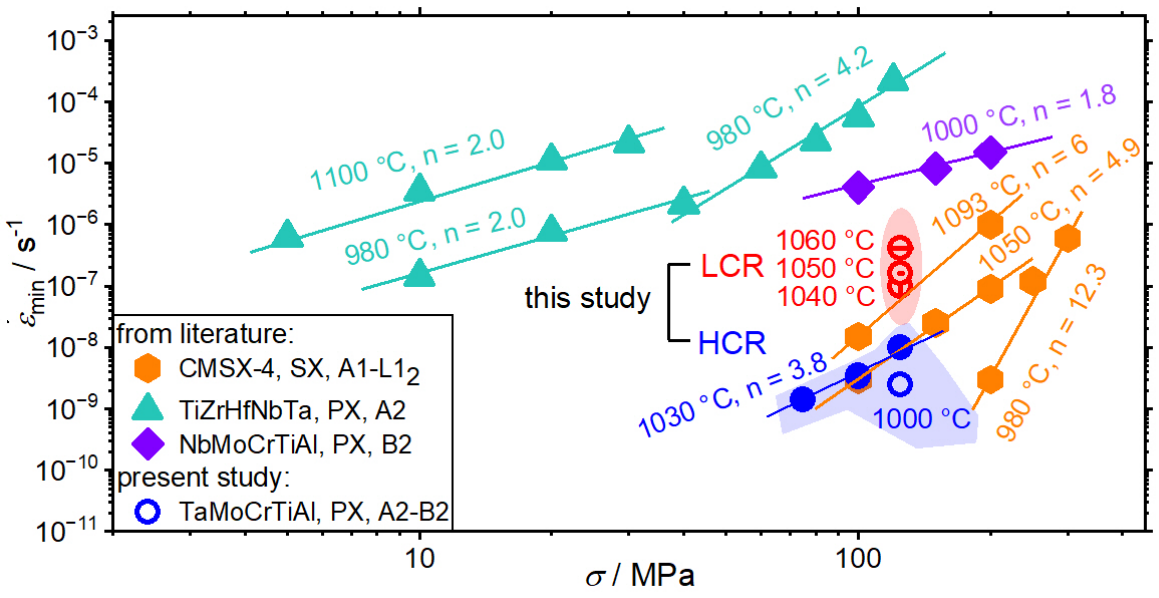

Fig. 5. Comparison of strain rate vs. applied stress for investigated poly-crystalline TMT-8Cr-10Al alloy and poly-crystalline B2 NbMoCrTiAl alloy [58], poly-crystalline A2 TiZrHfNbTa [29] as well as for a single-crystalline Ni-based superalloy CMSX-4.

3.3 Microstructure evolution after creep deformation

Fig. 6 (a-c) shows the SEM-BSE micrographs and the evolution of TMT-8Cr-10Al after creep deformation at 1000 °C/125 MPa for strains of 0.5, 0.6, and 0.8%, respectively. The compression direction in the micrographs is horizontal. In the absence of creep deformation, the size of the B2 precipitates were previously reported to increase with increasing heat treatment times while the phase fraction of the precipitates was found to initially increase (the growth regime) before saturating after a certain annealing time (the coarsening regime) [28]. To illustrate the difference in the microstructure after annealing without creep deformation, samples were heat treated at 1000 °C for times equivalent to each creep test, as displayed in Fig. 6 (d-f).

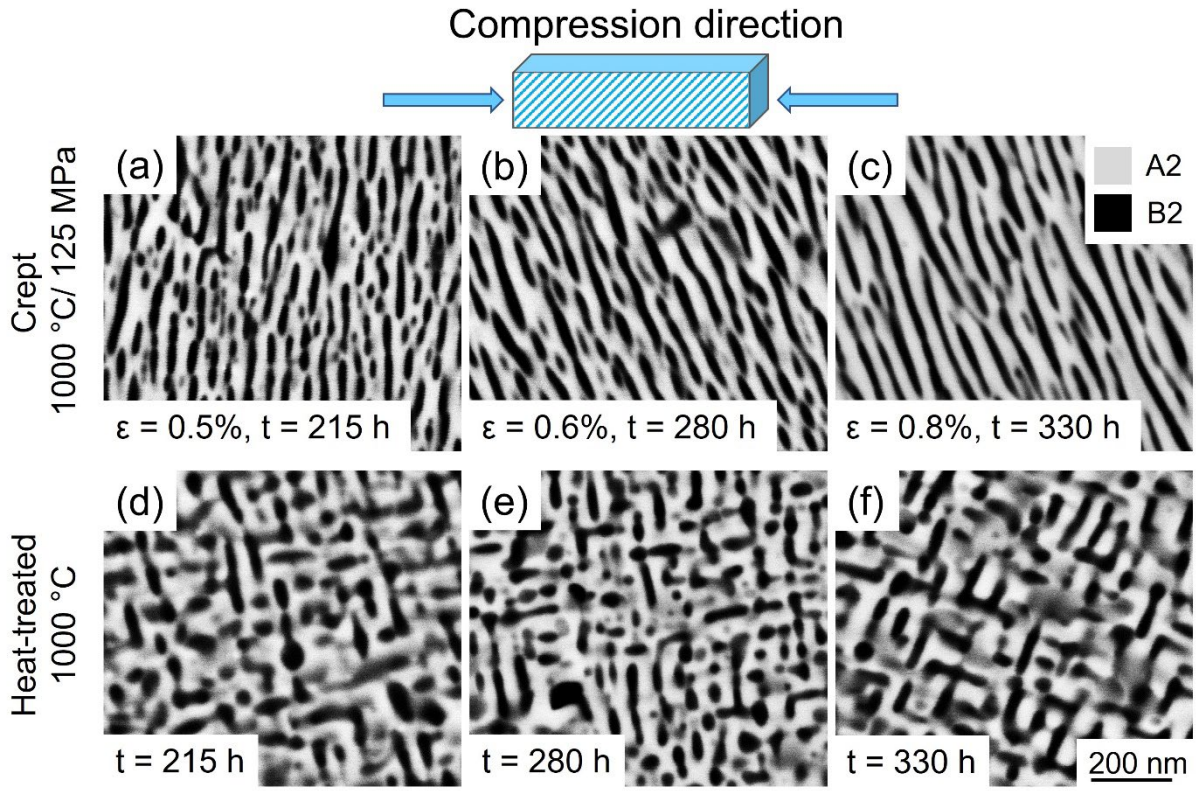

Fig. 6. SEM-BSE micrographs showing microstructure evolution of TMT-8Cr-10Al alloy after creep tests at 1000 °C with a stress of 125 MPa and strains of: (a) 0.5%, (b) 0.6%, and (c) 0.8% as well as heat treatments at 1000 °C for: (d) 215 h, (e) 280 h, and (f) 330 h.

Fig. 7 depicts the changes in phase fraction of the precipitates at 1000 °C after creep and heat treatment for the different times and microstructures as revealed in Fig. 6. The increase in the phase fraction of the precipitates (calculated by area fraction in the SEM-BSE images) is evident in both, the crept and annealed samples. The phase fraction of precipitates increases over the tested time range, which indicates that the precipitates are still in the process of growth during the creep deformation as opposed to being in the coarsening process where a saturation of the precipitate fraction is expected. Furthermore, it can be seen from Fig. 7 that the precipitate growth is accelerated under creep conditions as compared to the conditions without plastic deformation imposed. The impact of additional deformation on the kinetics of precipitate growth can be attributed to the dislocation activity. Dislocations might act as heterogeneous nucleation sites as well as fast diffusion paths enhancing both, the nucleation and growth rates, respectively.

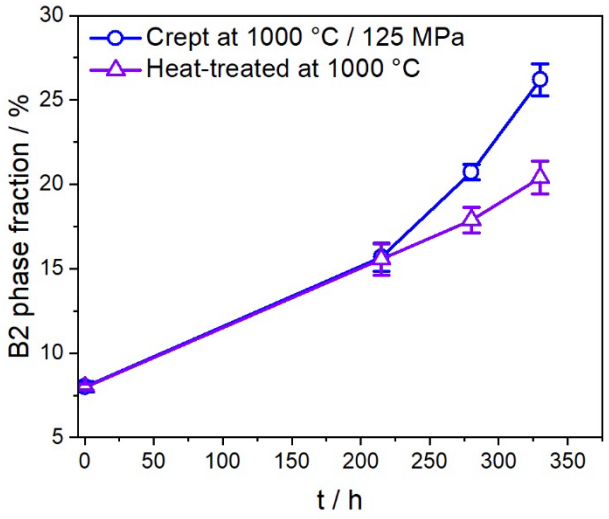

Fig. 7. The phase fraction of B2 precipitates of TMT-8Cr-10Al at 1000 °C as a function of time of creep deformation (125 MPa) and annealing.

Besides the change in the fraction of the precipitates, the other notable difference between the crept and the annealed samples is in the morphology of the precipitates. In contrast to the heat-treated samples, the crept microstructures show a pronounced directional growth similar to the rafting phenomenon of precipitates in Al-$L1_2$ Ni-based superalloys. As mentioned earlier, the majority of the creep experiments on Al-$L1_2$ Ni-based superalloys were performed on ⟨100⟩ oriented single crystals. Since the samples used in our study are poly-crystalline, the correlation between the grain orientation, and the angle between the loading direction to the rafted precipitates is not straightforward. In A1-$L1_2$ CMSX-4, the resistance to creep in compression was reported to decrease in the sequence of ⟨100⟩, ⟨111⟩ and ⟨110⟩ directions parallel to the compression direction. This was attributed to the resolved shear stresses on slip systems for each orientation [59]. This differentiation is also of great relevance for creep studies in our poly-crystalline A2-B2 alloy since grain orientation might affect the creep response. Due to the absence of single crystalline samples, the direct correlation of creep resistance to the grain orientation is not possible since the obtained creep response are a result of the entire sample containing multiple grains of different orientation.

In order to study such a correlation, EBSD investigations were performed on samples crept at 1000 °C up to a strain of 0.5% (Fig. 8 (a)) and 0.8% (Fig. 8 (b)). The relationship between the loading direction and the surface on which EBSD was performed is illustrated in Fig. 8. The IPF map is plotted such that the directions are color-coded by the standard triangle of the compression direction in the inset. A few grains in the IPF map for each sample in Fig. 8 are selected (marked 1-4) to represent the orientations close to the corners of the standard triangle. The SEM-BSE images highlighting the rafting direction for the grains marked in Fig. 8 (a) and (b) are shown in Fig. 8 (a1) to (a4) and (b1) to (b4), respectively.

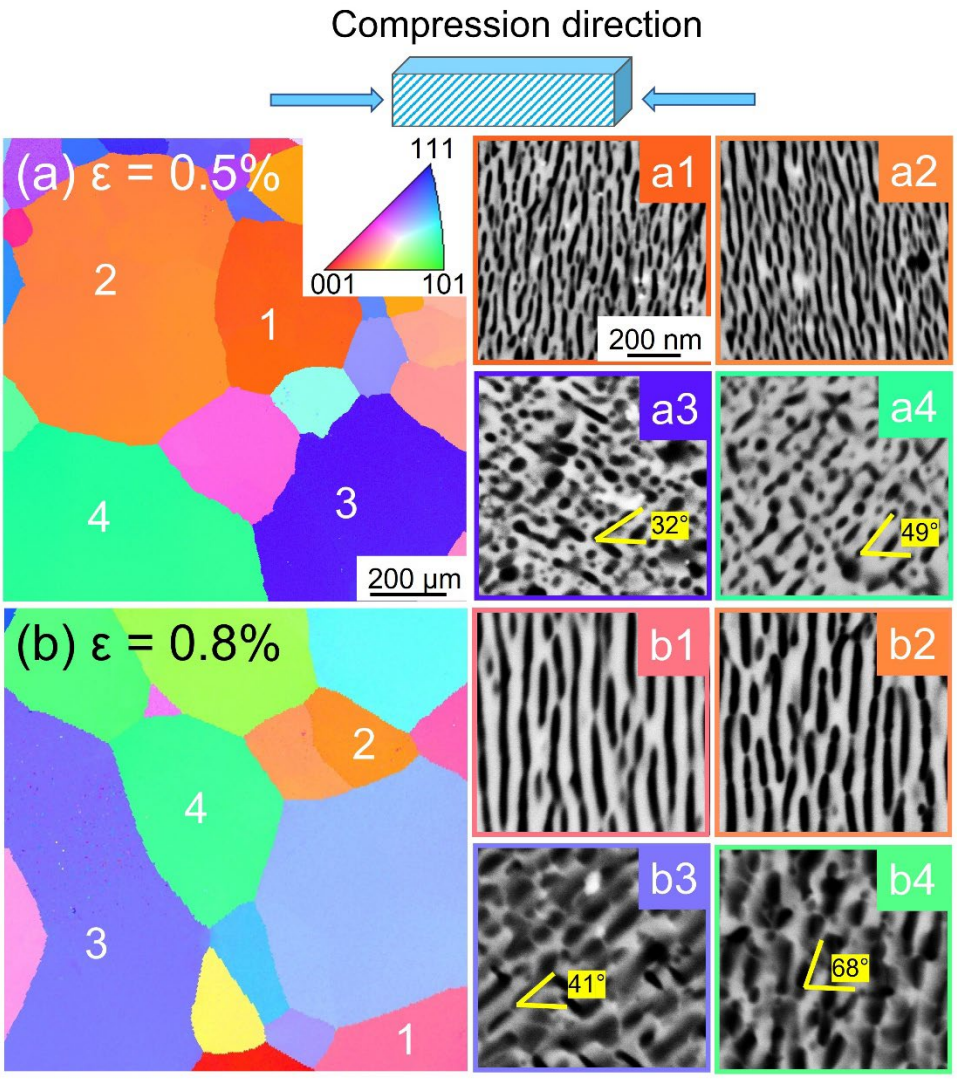

Fig. 8. EBSD-IPF maps and the direction of rafting (1-4) in each corresponding grain. The creep tests were performed at 1000 °C for total strains of (a) 0.5% and (b) 0.8%.

As was summarized in Table 1, N-type rafting is observed when the sign of lattice misfit (+/−) is opposite to the loading type, e.g. compression (−)/tension (+). For the present case, this was verified as the lattice misfit of the B2 precipitates was observed to be positive (+) via HR-TEM in Fig. 3(b-c) and compression (−) was applied during creep. Two observations in this regard are important to conclude from Fig. 8. Firstly, the direction of rafting with respect to the compression direction is not unique and strongly depends on the grain orientation. Secondly, the direction of rafting is clearly perpendicular to the compression direction for the grains where the ⟨100⟩ direction is parallel to the compression direction. This observation is similar to the creep results in poly-crystalline Co-based superalloys, where rafting perpendicular to the compression direction was observed only for ⟨100⟩ oriented grains [36,45]. The angles between the rafted structure and the loading direction lie between 45 to 70° in grain orientations other than ⟨100⟩. Thus, it can be concluded that similar to the A1-$L1_2$ Ni- and Co-based superalloys, the direction of the rafted microstructure can be predicted following the same scheme presented in Table 1 for grains whose ⟨100⟩ directions are close or even parallel to the compression direction.

Since a significant reduction of creep resistance was obtained at temperatures ≥ 1040 °C (LCR in Fig. 4) with increasing temperature as shown in Fig. 4 (b), it is required to correlate the evolution of microstructure in the creep samples at higher temperatures. Fig. 9 (a-c) shows the microstructural evolution of crept samples at temperatures ranging from 1030 to 1060 °C at a constant stress of 125 MPa.

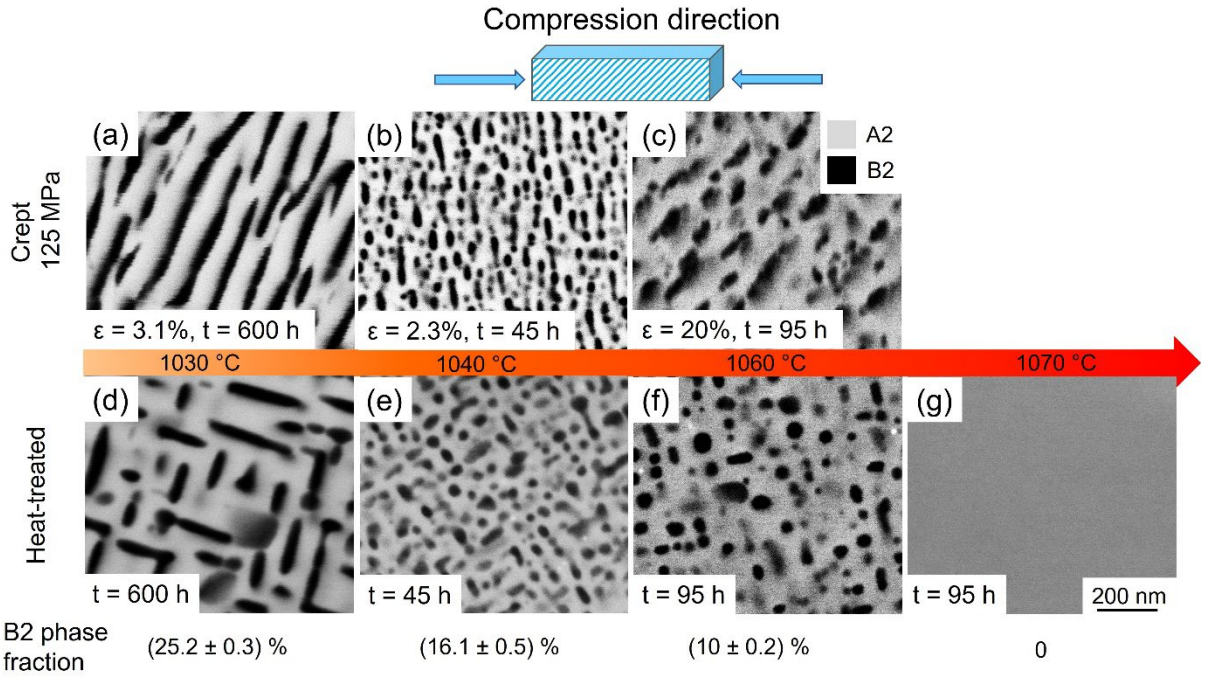

Fig. 9. Microstructure evolution of TMT-8Cr-10Al alloy after creep tests and heat treatments: (a) 1030 °C/125 MPa/3.1%, (b) 1040 °C/125 MPa/2.3%, (c) 1060 °C/125 MPa/20%. (d) 1030 °C/600 h, (e) 1040 °C/45 h, (f) 1060 °C/95 h and (g) 1070 °C/95 h. Same magnification used in all images.

The microstructural features after creep at 1030 °C are quite similar to those at 1000 °C in terms of rafting of the precipitates. In contrast, the microstructure for sample crept at 1040 °C and higher appears different. The microstructure of the sample crept at 1060 °C, shows a much smaller rafted length as compared to the sample crept at 1030 °C, even though the total strain is over six times larger. It must be noted however that the creep time for each temperature condition is not the same. The samples for the microstructure Fig. 9 (a-c) were cooled inside the furnace after the completion of the creep experiments. This furnace cooling allows the precipitates to re-nucleate during the cooling process. Thus, the microstructures shown in Fig. 9 (a-c) may not depict the actual state of the samples during the creep experiments. In order to visualize the state of the sample as it would have been during the creep experiments, samples were additionally annealed at temperatures and times equivalent to the creep tests and then subsequently quenched in water. These micrographs are shown in Fig. 9 (d-g).

At 1060 °C the samples still contain B2 precipitates after being annealed for 95 h. In order to determine the temperature where the precipitates dissolve completely, one sample was also annealed at 1070 °C for 95 h (similar to the time for 1060 °C) wherein no precipitates were found (Fig. 9 (g)). It may further be noted that although 1060 °C (Fig. 9 (f)) is a bit higher than the previously reported 1055 °C solvus temperature of B2 in TMT-8Cr-10Al but still exhibits B2 precipitates. Single-phase A2 devoid of B2 precipitates in TMT-8Cr-10Al is only verified for 1070 °C in these experiments. There are many aspects which can explain this deviation. Firstly, the determination of the solvus temperature in Ref. [27] involves the analysis of the peak temperature of the heat signature in the DSC experiment. However, the

formation of the present microstructure involves two reaction types, e.g. a diffusion-controlled 1st order phase separation as well as a 2nd order ordering reaction [27]. The heat signatures of both are superimposed in the DSC experiments. While 2nd order transitions are indeed evaluated for their characteristic peak temperatures [60], diffusion-controlled 1st order phase transformations need to be characterized by their extrapolated peak-onset temperatures [60–63]. As the lambda-shaped heat signature of the 2nd order phase transformation spans down to 800 °C in the case of TMT-8Cr-10Al, the onset of the diffusion-controlled, characteristic temperatures of the 1st order phase separation can only be estimated from DSC experiments by the evaluation of the peak temperature. Secondly, it is important to consider that the dissolution of the precipitates is a diffusion-controlled process, hence the dissolution of the precipitates beyond the solvus temperature is also dependent on the time of annealing. Taking these two aspects into account in addition to the possible errors in the different thermocouples used in the DSC and furnaces used for annealing and in the creep testing device, it can be said the actual solvus temperature would very close to the previously reported solvus temperature of 1055 °C with a possible difference of 5 to 10 K.

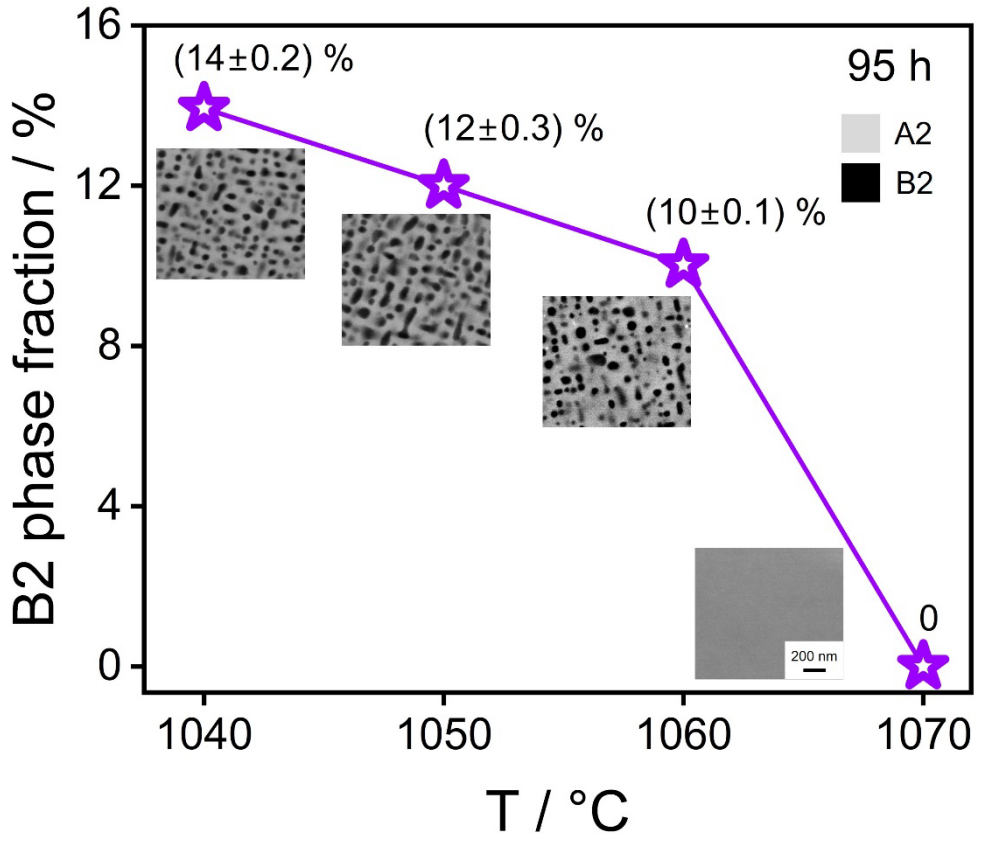

Fig. 10. The phase fraction of B2 precipitates of TMT-8Cr-10Al annealed at 1040 °C to 1070 °C for 95 h. Same magnification used in all images.

Although B2 precipitates were observed up to annealing temperatures of 1060 °C, not just the presence of precipitates but the phase fraction of the precipitates also plays a key role in determining the creep response of the TMT-8Cr-10Al. Since, the annealing times for Fig. 9 (d-g) are not constant, additional annealing treatments were conducted at 1040 °C and 1050 °C for 95 h in order to quantitatively analyze the temperature depending volume fraction of the precipitates. These results are plotted in Fig. 10. It is clear that although the precipitates are still present at 1060 °C, the volume fraction decreases sharply from 1040 °C. The higher $\dot{\varepsilon}_{\mathrm{min}}$ observed in the LCR regime (Fig. 4 (b)) is, hence, mainly caused by a

reduction in the B2 phase fraction at temperatures close to the actual solvus temperature. It is relevant to note that creep tests at 125 MPa in the single-phase A2 region ≥ 1070 °C repeatedly failed by too fast creep rates. Apart from benefits of the creep performance of TMT-8Cr-10Al over poly-crystalline A2, poly-crystalline B2 and also single-crystalline CMSX-4 as showcased in Section 3.2, the relevance of precipitation strengthening for causing these excellent creep properties is highlighted by these observations.

4. Conclusions

The poly-crystalline refractory high entropy alloy TMT-8Cr-10Al (at. %) with a two-phase microstructure consisting of a disordered A2 matrix and ordered B2 precipitates shows a promising creep resistance at high temperatures.

Compared to poly-crystalline, single-phase A2 and B2 RHEA, it can be concluded that

- Precipitation strengthening of RCCA by B2 precipitates in A2 matrix is effective as TMT-8Cr-10Al exhibits a substantially higher creep resistance over single, poly-crystalline A2 and B2 RHEA. The difference amounts to about three to four orders of magnitude in creep rate at comparable stress and temperature.

Compared to state-of-the-art, single-crystalline A1-$L1_2$ CMSX-4, it can be concluded that

- TMT-8Cr-10Al exhibits a comparable minimum creep rate compared to CMSX-4 in the stress range of 75 to 125 MPa and temperatures ranging from 1000 to 1030 °C.

- The comparable creep resistance under these testing conditions is remarkable as TMT-8Cr-10Al is poly-crystalline compared to the single-crystalline CMSX-4. Furthermore, TMT-8Cr-10Al tested at 1030 °C is operated much closer to its solvus temperature of 1060 to 1070 °C compared to CMSX-4 with 1280 °C.

Regarding the microstructural changes upon creep and annealing, the following conclusions can be drawn:

- A directional coarsening or rafting of precipitates microstructure of TMT-8Cr-10Al is observed after crept at 1000 and 1030 °C with a stress of 125 MPa. The combination of positive lattice misfit and compression loading causes N-type rafting of the microstructure in grains with the ⟨100⟩ parallel to the loading direction consistent with the established theories on the formation of rafted microstructures in Ni- and Co-based superalloys.

- A reduction in the creep resistance observed at higher temperatures close to the solvus temperature is correlated to a significant reduction of the B2 phase fraction.

Acknowledgments

The financial support by the Deutsche Forschungsgemeinschaft (DFG), grant no. HE 1872/34-2 is gratefully acknowledged. The authors are grateful for the chemical analysis by ICP-OES carried out at the Institute for Applied Materials (IAM-AWP), Karlsruhe Institute of Technology (KIT). LY is financially supported by China Scholarship Council (CSC) with No. 202207000023. AC gratefully acknowledges financial support from the Infosys Foundation, Bangalore. AP and AC also recognize the Advanced Centre for Microscopy and Microanalysis (AFMM) and its staff at IISc, Bengaluru, for

providing access to the research facilities. RJV acknowledges the support by the Alexander von Humboldt Foundation.

Data Availability Statement

The data presented in this study are available in KITopen at https://doi.org/10.35097/0mv9vfxr8rjxbpdj under CC BY-SA 4.0 license. Further information is available upon request with alexander.kauffmann@kit.edu.

References

[1] J.-W. Yeh, S.-K. Chen, S.-J. Lin, J.-Y. Gan, T.-S. Chin, T.-T. Shun, C.-H. Tsau, S.-Y. Chang, Nanostructured High-Entropy Alloys with Multiple Principal Elements: Novel Alloy Design Concepts and Outcomes, Advanced Engineering Materials 6 (2004) 299–303. https://doi.org/10.1002/adem.200300567.

[2] J.-W. Yeh, S.-J. Lin, T.-S. Chin, J.-Y. Gan, S.-K. Chen, T.-T. Shun, C.-H. Tsau, S.-Y. Chou, Formation of simple crystal structures in Cu-Co-Ni-Cr-Al-Fe-Ti-V alloys with multiprincipal metallic elements, Metallurgical and Materials Transactions A 35 (2004) 2533–2536. https://doi.org/10.1007/s11661-006-0234-4.

[3] B. Cantor, I.T.H. Chang, P. Knight, A.J.B. Vincent, Microstructural development in equiatomic multicomponent alloys, Materials Science and Engineering: A 375–377 (2004) 213–218. https://doi.org/10.1016/j.msea.2003.10.257.

[4] O.N. Senkov, G.B. Wilks, D.B. Miracle, C.P. Chuang, P.K. Liaw, Refractory high-entropy alloys, Intermetallics 18 (2010) 1758–1765. https://doi.org/10.1016/j.intermet.2010.05.014.

[5] O.N. Senkov, G.B. Wilks, J.M. Scott, D.B. Miracle, Mechanical properties of Nb25Mo25Ta25W25 and V20Nb20Mo20Ta20W20 refractory high entropy alloys, Intermetallics 19 (2011) 698–706. https://doi.org/10.1016/j.intermet.2011.01.004.

[6] O.N. Senkov, J.M. Scott, S.V. Senkova, D.B. Miracle, C.F. Woodward, Microstructure and room temperature properties of a high-entropy TaNbHfZrTi alloy, Journal of Alloys and Compounds 509 (2011) 6043–6048. https://doi.org/10.1016/j.jallcom.2011.02.171.

[7] O.N. Senkov, J.M. Scott, S.V. Senkova, F. Meisenkothen, D.B. Miracle, C.F. Woodward, Microstructure and elevated temperature properties of a refractory TaNbHfZrTi alloy, Journal of Materials Science 47 (2012) 4062–4074. https://doi.org/10.1007/s10853-012-6260-2.

[8] B. Gorr, S. Schellert, F. Müller, H.-J. Christ, A. Kauffmann, M. Heilmaier, Current Status of Research on the Oxidation Behavior of Refractory High Entropy Alloys, Advanced Engineering Materials 23 (2021) 2001047. https://doi.org/10.1002/adem.202001047.

[9] B. Gorr, M. Azim, H.-J. Christ, T. Mueller, D. Schliephake, M. Heilmaier, Phase equilibria, microstructure, and high temperature oxidation resistance of novel refractory high-entropy alloys, Journal of Alloys and Compounds 624 (2015) 270–278.

[10] B. Gorr, F. Müller, M. Azim, H.-J. Christ, T. Müller, H. Chen, A. Kauffmann, M. Heilmaier, High-Temperature Oxidation Behavior of Refractory High-Entropy Alloys: Effect of Alloy Composition, Oxid Met 88 (2017) 339–349. https://doi.org/10.1007/s11085-016-9696-y.

[11] C.M. Liu, H.M. Wang, S.Q. Zhang, H.B. Tang, A.L. Zhang, Microstructure and oxidation behavior of new refractory high entropy alloys, Journal of Alloys and Compounds 583 (2014) 162–169.

[12] S. Schellert, B. Gorr, S. Laube, A. Kauffmann, M. Heilmaier, H.J. Christ, Oxidation mechanism of refractory high entropy alloys Ta-Mo-Cr-Ti-Al with varying Ta content, Corrosion Science 192 (2021) 109861. https://doi.org/10.1016/j.corsci.2021.109861.

[13] B. Gorr, F. Müller, S. Schellert, H.-J. Christ, H. Chen, A. Kauffmann, M. Heilmaier, A new strategy to intrinsically protect refractory metal based alloys at ultra high temperatures, Corrosion Science 166 (2020) 108475. https://doi.org/10.1016/j.corsci.2020.108475.

[14] S. Schellert, B. Gorr, H.-J. Christ, C. Pritzel, S. Laube, A. Kauffmann, M. Heilmaier, The Effect of Al on the Formation of a CrTaO4 Layer in Refractory High Entropy Alloys Ta-Mo-Cr-Ti-xAl, Oxidation of Metals 96 (2021) 333–345. https://doi.org/10.1007/s11085-021-10046-7.

[15] S. Schellert, M. Weber, H.J. Christ, C. Wiktor, B. Butz, M.C. Galetz, S. Laube, A. Kauffmann, M. Heilmaier, B. Gorr, Formation of rutile (Cr,Ta,Ti)O2 oxides during oxidation of refractory high entropy alloys in Ta-Mo-Cr-Ti-Al system, Corrosion Science 211 (2023) 110885. https://doi.org/10.1016/j.corsci.2022.110885.
[16] H. Chen, Kauffmann, A., B. Gorr, D. Schliephake, C. Seemüller, J.N. Wagner, H.-J. Christ, M. Heilmaier, Microstructure and mechanical properties at elevated temperatures of a new Al-containing refractory high-entropy alloy Nb-Mo-Cr-Ti-Al, Journal of Alloys and Compounds 661 (2016) 206–215.
[17] H. Chen, A. Kauffmann, S. Laube, I.-C. Choi, R. Schwaiger, Y. Huang, K. Lichtenberg, F. Müller, B. Gorr, H.-J. Christ, M. Heilmaier, Contribution of Lattice Distortion to Solid Solution Strengthening in a Series of Refractory High Entropy Alloys, Metallurgical and Materials Transactions A 49 (2018) 772–781. https://doi.org/10.1007/s11661-017-4386-1.
[18] H. Chen, A. Kauffmann, S. Seils, T. Boll, C.H. Liebscher, I. Harding, K.S. Kumar, D.V. Szabó, S. Schlabach, S. Kauffmann-Weiss, F. Müller, B. Gorr, H.-J. Christ, M. Heilmaier, Crystallographic ordering in a series of Al-containing refractory high entropy alloys Ta–Nb–Mo–Cr–Ti–Al, Acta Materialia 176 (2019) 123–133. https://doi.org/10.1016/j.actamat.2019.07.001.
[19] S. Laube, H. Chen, A. Kauffmann, S. Schellert, F. Müller, B. Gorr, J. Müller, B. Butz, H.-J. Christ, M. Heilmaier, Controlling crystallographic ordering in Mo–Cr–Ti–Al high entropy alloys to enhance ductility, Journal of Alloys and Compounds 823 (2020) 153805. https://doi.org/10.1016/j.jallcom.2020.153805.
[20] S. Laube, G. Winkens, A. Kauffmann, J. Li, C. Kirchlechner, M. Heilmaier, Strength of Disordered and Ordered Al-Containing Refractory High-Entropy Alloys, Advanced Engineering Materials n/a (2024) 2301797. https://doi.org/10.1002/adem.202301797.
[21] D.B. Miracle, M.-H. Tsai, O.N. Senkov, V. Soni, R. Banerjee, Refractory high entropy superalloys (RSAs), Scripta Materialia 187 (2020) 445–452. https://doi.org/10.1016/j.scriptamat.2020.06.048.
[22] D.-M. Jin, Z.-H. Wang, J.-F. Li, B. Niu, Q. Wang, Formation of coherent BCC/B2 microstructure and mechanical properties of Al–Ti–Zr–Nb–Ta–Cr/Mo light-weight refractory high-entropy alloys, Rare Met. 41 (2022) 2886–2893. https://doi.org/10.1007/s12598-022-01971-w.
[23] N. Yurchenko, E. Panina, D. Shaysultanov, S. Zherebtsov, N. Stepanov, Refractory high entropy alloy with ductile intermetallic B2 matrix/hard bcc particles and exceptional strain hardening capacity, Materialia 20 (2021) 101225.
[24] F. Körmann, T. Kostiuchenko, A. Shapeev, J. Neugebauer, B2 ordering in body-centered-cubic AlNbTiV refractory high-entropy alloys, Phys. Rev. Materials 5 (2021) 053803. https://doi.org/10.1103/PhysRevMaterials.5.053803.
[25] E. Zhang, Y. Tang, M. Wen, A. Obaied, I. Roslyakova, L. Zhang, On phase stability of Mo-Nb-Ta-W refractory high entropy alloys, International Journal of Refractory Metals and Hard Materials 103 (2022) 105780.
[26] E.A. Lass, On the Thermodynamics and Phase Transformation Pathways in BCC-B2 Refractory Compositionally Complex Superalloys, Metallurgical and Materials Transactions A 53 (2022) 4481–4498. https://doi.org/10.1007/s11661-022-06844-6.
[27] S. Laube, S. Schellert, A. Srinivasan Tirunilai, D. Schliephake, B. Gorr, H.-J. Christ, A. Kauffmann, M. Heilmaier, Microstructure tailoring of Al-containing compositionally complex alloys by controlling the sequence of precipitation and ordering, Acta Materialia 218 (2021) 117217. https://doi.org/10.1016/j.actamat.2021.117217.
[28] S. Laube, A. Kauffmann, S. Schellert, S. Seils, A.S. Tirunilai, C. Greiner, Y.M. Eggeler, B. Gorr, H.-J. Christ, M. Heilmaier, Formation and thermal stability of two-phase microstructures in Al-containing refractory compositionally complex alloys, Science and Technology of Advanced Materials 23 (2022) 692–706. https://doi.org/10.1080/14686996.2022.2132118.
[29] C. Gadelmeier, Y. Yang, U. Glatzel, E.P. George, Creep strength of refractory high-entropy alloy TiZrHfNbTa and comparison with Ni-base superalloy CMSX-4, Cell Reports Physical Science 3 (2022) 100991. https://doi.org/10.1016/j.xcrp.2022.100991.
[30] C.-J. Liu, C. Gadelmeier, S.-L. Lu, J.-W. Yeh, H.-W. Yen, S. Gorsse, U. Glatzel, A.-C. Yeh, Tensile creep behavior of HfNbTaTiZr refractory high entropy alloy at elevated temperatures, Acta Materialia 237 (2022) 118188. https://doi.org/10.1016/j.actamat.2022.118188.

[31] A. Epishin, B. Fedelich, G. Nolze, S. Schriever, T. Feldmann, M.F. Ijaz, B. Viguier, D. Poquillon, Y. Le Bouar, A. Ruffini, A. Finel, Creep of Single Crystals of Nickel-Based Superalloys at Ultra-High Homologous Temperature, Metallurgical and Materials Transactions A 49 (2018) 3973–3987. https://doi.org/10.1007/s11661-018-4729-6.
[32] F.R.N. Nabarro, Rafting in Superalloys, Metall Mater Trans A 27 (1996) 513–530. https://doi.org/10.1007/BF02648942.
[33] W. Xia, X. Zhao, L. Yue, Z. Zhang, Microstructural evolution and creep mechanisms in Ni-based single crystal superalloys: A review, Journal of Alloys and Compounds 819 (2020) 152954. https://doi.org/10.1016/j.jallcom.2019.152954.
[34] H. Mughrabi, The importance of sign and magnitude of γ/γ′ lattice misfit in superalloys—with special reference to the new γ′-hardened cobalt-base superalloys, Acta Materialia 81 (2014) 21–29. https://doi.org/10.1016/j.actamat.2014.08.005.
[35] J.K. Tien, R.P. Gamble, Effects of stress coarsening on coherent particle strengthening, Metall Trans 3 (1972) 2157–2162. https://doi.org/10.1007/BF02643227.
[36] A. Bauer, S. Neumeier, F. Pyczak, M. Göken, Creep strength and microstructure of polycrystalline γ'–strengthened cobalt-base superalloys, Superalloys 12 (2012) 695–703.
[37] A.B. Parsa, D. Bürger, T.M. Pollock, G. Eggeler, Misfit and the mechanism of high temperature and low stress creep of Ni-base single crystal superalloys, Acta Materialia 264 (2024) 119576. https://doi.org/10.1016/j.actamat.2023.119576.
[38] T. Murakumo, T. Kobayashi, Y. Koizumi, H. Harada, Creep behaviour of Ni-base single-crystal superalloys with various γ′ volume fraction, Acta Materialia 52 (2004) 3737–3744. https://doi.org/10.1016/j.actamat.2004.04.028.
[39] L. Agudo Jácome, P. Nörtershäuser, J.-K. Heyer, A. Lahni, J. Frenzel, A. Dlouhy, C. Somsen, G. Eggeler, High-temperature and low-stress creep anisotropy of single-crystal superalloys, Acta Materialia 61 (2013) 2926–2943. https://doi.org/10.1016/j.actamat.2013.01.052.
[40] L. Cui, J. Yu, J. Liu, X. Sun, Microstructural evolutions and fracture behaviors of a newly developed nickel-base superalloy during creep deformation, Journal of Alloys and Compounds 746 (2018) 335–349. https://doi.org/10.1016/j.jallcom.2018.02.295.
[41] A. Altincekic, E. Balikci, Precipitate Rafting in a Polycrystalline Superalloy During Compression Creep, Metall Mater Trans A 45 (2014) 5923–5936. https://doi.org/10.1007/s11661-014-2558-9.
[42] M.S. Titus, A. Suzuki, T.M. Pollock, Creep and directional coarsening in single crystals of new γ–γ′ cobalt-base alloys, Scripta Materialia 66 (2012) 574–577. https://doi.org/10.1016/j.scriptamat.2012.01.008.
[43] F. Xue, H.J. Zhou, Q.Y. Shi, X.H. Chen, H. Chang, M.L. Wang, Q. Feng, Creep behavior in a γ′ strengthened Co–Al–W–Ta–Ti single-crystal alloy at 1000 °C, Scripta Materialia 97 (2015) 37–40. https://doi.org/10.1016/j.scriptamat.2014.10.015.
[44] F. Pyczak, A. Bauer, M. Göken, S. Neumeier, U. Lorenz, M. Oehring, N. Schell, A. Schreyer, A. Stark, F. Symanzik, Plastic deformation mechanisms in a crept L12 hardened Co-base superalloy, Materials Science and Engineering: A 571 (2013) 13–18. https://doi.org/10.1016/j.msea.2013.02.007.
[45] A. Bauer, S. Neumeier, F. Pyczak, R.F. Singer, M. Göken, Creep properties of different γ′-strengthened Co-base superalloys, Materials Science and Engineering: A 550 (2012) 333–341. https://doi.org/10.1016/j.msea.2012.04.083.
[46] D. Schliephake, A.E. Medvedev, M.K. Imran, S. Obert, D. Fabijanic, M. Heilmaier, A. Molotnikov, X. Wu, Precipitation behaviour and mechanical properties of a novel Al0.5MoTaTi complex concentrated alloy, Scripta Materialia 173 (2019) 16–20. https://doi.org/10.1016/j.scriptamat.2019.07.033.
[47] N. Yurchenko, E. Panina, Ł. Rogal, L. Shekhawat, S. Zherebtsov, N. Stepanov, Unique precipitations in a novel refractory Nb-Mo-Ti-Co high-entropy superalloy, Materials Research Letters 10 (2022) 78–87. https://doi.org/10.1080/21663831.2021.2022033.
[48] C.H. Belcher, D. Kamp, S. To, Y. Lu, D. Chassaing, T. Boll, B.E. MacDonald, E.M.Y. Lee, D. Apelian, E.J. Lavernia, The Origin and Control of Interstitial Impurities in Refractory Complex Concentrated Alloys, (2024). https://doi.org/10.2139/ssrn.4865723.

[49] R.W. Balluffi, L.L. Seigle, Growth of voids in metals during diffusion and creep, Acta Metallurgica 5 (1957) 449–454. https://doi.org/10.1016/0001-6160(57)90063-9.
[50] W. Blum, P. Eisenlohr, F. Breutinger, Understanding creep—a review, Metallurgical and Materials Transactions A 33 (2002) 291–303. https://doi.org/10.1007/s11661-002-0090-9.
[51] H. Mughrabi, Revisiting "Steady-State" Monotonic and Cyclic Deformation: Emphasizing the Quasi-Stationary State of Deformation, Metallurgical and Materials Transactions A 51 (2020) 1441–1456. https://doi.org/10.1007/s11661-019-05618-x.
[52] A.K. Mukherjee, J.E. Bird, J.E. Dorn, Experimental correlations for high-temperature creep, (1968). https://escholarship.org/content/qt31p4z5v2/qt31p4z5v2.pdf (accessed July 23, 2024).
[53] Self-diffusion in pure metals - ScienceDirect, (n.d.). https://www.sciencedirect.com/science/article/pii/0022311578902349 (accessed July 18, 2024).
[54] H. Nakajima, K. Nonaka, W. Sprengel, M. Koiwa, Self-diffusion and interdiffusion in intermetallic compounds, Materials Science and Engineering: A 239–240 (1997) 819–827. https://doi.org/10.1016/S0921-5093(97)00672-2.
[55] F.R.N. Nabarro, Grain size, stress, and creep in polycrystalline solids, Physics of the Solid State 42 (2000) 1456–1459. https://doi.org/10.1134/1.1307052.
[56] M. Heilmaier, M. Krüger, H. Saage, J. Rösler, D. Mukherji, U. Glatzel, R. Völkl, R. Hüttner, G. Eggeler, Ch. Somsen, T. Depka, H.-J. Christ, B. Gorr, S. Burk, Metallic materials for structural applications beyond nickel-based superalloys, JOM 61 (2009) 61–67. https://doi.org/10.1007/s11837-009-0106-7.
[57] D.K. Matlock, W.D. Nix, The effect of sample size on the steady state creep characteristics of Ni-6 pct W, Metall Trans 5 (1974) 1401–1412. https://doi.org/10.1007/BF02646626.
[58] Hans Chen, Alexander Kauffmann, Martin Heilmaier, Unpublished results, (2019).
[59] W. Österle, D. Bettge, B. Fedelich, H. Klingelhöffer, Modelling the orientation and direction dependence of the critical resolved shear stress of nickel-base superalloy single crystals, Acta Materialia 48 (2000) 689–700. https://doi.org/10.1016/S1359-6454(99)00404-8.
[60] F. Stein, M. Palm, Re-determination of transition temperatures in the Fe–Al system by differential thermal analysis, International Journal of Materials Research 98 (2007) 580–588. https://doi.org/10.3139/146.101512.
[61] G.W.H. Höhne, H.K. Cammenga, W. Eysel, E. Gmelin, W. Hemminger, The temperature calibration of scanning calorimeters, Thermochimica Acta 160 (1990) 1–12. https://doi.org/10.1016/0040-6031(90)80235-Q.
[62] E. Gmelin, St.M. Sarge, Calibration of differential scanning calorimeters, 67 (1995) 1789–1800. https://doi.org/10.1351/pac199567111789.
[63] G.W.H. Höhne, Remarks on the calibration of differential scanning calorimeters, Journal of Thermal Analysis 37 (1991) 1987–2000. https://doi.org/10.1007/BF01912232.